

Valley polarization, magnetization, and superconductivity in bilayer graphene near the van Hove singularity

Alex Friedlan, Heqiu Li, and Hae-Young Kee*

*Department of Physics and Centre for Quantum Materials, University of Toronto,
60 St. George Street, Toronto, Ontario, Canada, M5S 1A7*

The discovery of Mott insulators and superconductivity in twisted bilayer graphene has ignited intensive research into strong correlation effects in other stacking geometries. Bernal-stacked bilayer graphene (BBG), when subjected to a perpendicular electric field, exhibits phase transitions to a variety of broken-symmetry states. Notably, superconductivity emerges when BBG is in proximity to a heavy transition-metal dichalcogenide, highlighting the role of spin-orbit coupling (SOC). Here we investigate the origin of Ising SOC and its role in the competition between superconductivity and spin- and valley-polarized states in BBG. Starting from strong electron-electron interactions on the BBG lattice, we derive a low-energy effective model near the valleys that incorporates both density-density and spin-spin interactions. Using self-consistent mean-field theory, we map out the BBG phase diagram. Our findings reveal that near the van Hove filling, a mixed spin- and valley-polarized phase dominates over superconductivity. Away from the van Hove filling, a spin-polarized, spin-triplet superconducting state arises, characterized by an in-plane orientation of the magnetic moment and an out-of-plane orientation of the d -vector. Contrary to previous proposals, we find that Ising SOC favours spin-valley order while suppressing superconductivity near the van Hove singularity. We discuss other potential proximity effects and suggest directions for future studies.

I. INTRODUCTION

Twisted bilayer graphene has emerged as a popular platform for investigating strongly-correlated electronic states, primarily due to the appearance of flat Moiré bands at certain twist angles that amplify electron-electron interactions [1–3]. Until recently, the relatively innocuous platform of Bernal-stacked bilayer graphene (BBG) has been overlooked as a candidate material for correlated-electron physics.

Renewed interest in BBG was sparked by a pair of 2021 papers that observed a sequence of unusual symmetry-breaking electronic states as the bias field and electron density were tuned [4, 5]. Notably, when the BBG was subjected to an in-plane magnetic field, a region of superconductivity emerged within the phase diagram, pointing to unconventional superconductivity. A subsequent study found a similar enhancement of the superconducting state when the BBG was placed on a substrate of monolayer tungsten diselenide (WSe₂) [6]. Due to the low atomic mass of carbon, graphene exhibits intrinsically tiny spin-orbit coupling (SOC) [7–11]. However, when placed on a substrate with a heavy atom (i.e. tungsten), graphene experiences a proximity-induced SOC enhancement of up to two orders of magnitude [12–16]. SOC is believed to play a key role in the enhancement of the superconducting state [6, 17].

Recent experiments have further revealed the complex structure of the BBG phase diagram. In addition to superconductivity, spin- and valley-polarized phases [18–21], as well as exotic Wigner crystal and fractional quantum Hall states [22, 23] have been reported. One

study has even identified two separate superconducting regimes, one of which is argued to arise from a nematic normal state characterized by broken rotational symmetry [24]. Rhombohedral-stacked multilayer graphene, which shares many similarities with BBG, is also being vigorously explored [25–30].

Theoretical efforts to understand the various normal-state phases in BBG under a displacement field have also been undertaken [31–33]. These studies examine the normal-state phase diagrams in the presence of long-range Coulomb interactions [32, 33] and short-range Hund’s coupling [31], but do not address superconductivity. In addition, some work has focused on generic two-dimensional systems with spin and valley degrees of freedom [34, 35].

Several proposals have been put forward to explain the origin of superconductivity in the context of Ising SOC. A recent study proposed a mangon exchange mechanism for superconductivity arising from a spin-canted normal state, favouring s -wave pairing [36]. Another study has suggested combined p - and d -wave superconductivity that emerges from competition with an intravalley current density wave connecting the small Fermi pockets near the van Hove singularity [37]. f -wave superconductivity is also being explored [38, 39], and has been argued to be the most favourable superconducting channel [40, 41]. Clearly, the symmetry and origin of the superconducting state in BBG remain open questions requiring further exploration (see also Refs. [42–46]).

In this work, we examine the phase diagram of BBG near electron densities corresponding to the van Hove singularity (vHS) to explore the interplay of broken-symmetry phases. Our interacting model is based on the idea that, at low energies, the biased BBG lattice resembles a honeycomb lattice with a staggered sublattice potential, as studied in Ref. [47]. By applying

* hy.kee@utoronto.ca

a Schrieffer-Wolff transformation and incorporating on-site Hubbard, nearest-neighbor (NN), and next-nearest-neighbour (NNN) repulsive interactions, we obtain effective intervalley density-density and spin-spin interactions. The resulting effective Hamiltonian yields in valley-polarized, spin-polarized, and spin-triplet superconducting states. We perform self-consistent mean-field (MF) calculations with and without SOC to investigate the role of SOC in promoting superconductivity.

This paper is organized as follows. In Sec. II, we review the single-particle tight-binding Hamiltonian and examine the Fermi surface near half-filling. We then derive the proximity-induced SOC from the adjacent WSe₂ layer, starting from the atomic SOC in the tungsten *d* orbitals. In Sec. III, we introduce the interacting Hamiltonian on the BBG lattice, including electron-electron interactions up to next-nearest-neighbour distance. Performing a Schrieffer-Wolff transformation, we obtain the effective interacting Hamiltonian for electrons near the valleys, which takes the form of intervalley density-density and spin-spin interactions, akin to Hund's coupling in valley degrees of freedom. After introducing the MF order parameters in Sec. IV, we present the self-consistent MF phase diagram and results for a few representative parameter sets in Sec. V. Finally, in Sec. VI, we summarize our findings, discuss the implications, and outline open questions for future studies.

II. SINGLE-PARTICLE HAMILTONIAN

A. Tight-binding model

We begin with a short review on the tight-binding model of the BBG lattice. We consider bilayer graphene in an AB (Bernal) stacking arrangement as shown in Fig. 1. We include the NN intralayer hopping t_{\parallel} , the interlayer dimer hopping t_{\perp} , and the non-dimer interlayer hopping t_3 . To construct the tight-binding model, we introduce the creation (annihilation) operators $a_{l,\mathbf{k}}^{\dagger}$ and $b_{l,\mathbf{k}}^{\dagger}$ ($a_{l,\mathbf{k}}$ and $b_{l,\mathbf{k}}$), corresponding to sublattices *A* and *B*, respectively. The layers are indexed by $l \in \{1, 2\}$ and the associated momentum is denoted by \mathbf{k} . In addition to the hopping Hamiltonian, an external electric displacement field D is introduced perpendicular to the plane of the graphene, leading to the potential difference term $\mathcal{H}_D = D(n_1 - n_2)$, where n_l is the density operator for layer l .

Introducing the spinor $\tilde{\Psi}_{\mathbf{k}} = (a_{1,\mathbf{k}}, b_{1,\mathbf{k}}, a_{2,\mathbf{k}}, b_{2,\mathbf{k}})^T$, the Hamiltonian can be written $\mathcal{H}_0 = \sum_{\mathbf{k}} \tilde{\Psi}_{\mathbf{k}}^{\dagger} H_0(\mathbf{k}) \tilde{\Psi}_{\mathbf{k}}$, where $H_0(\mathbf{k})$ takes the explicit matrix form [48–50]

$$H_0(\mathbf{k}) = \begin{pmatrix} D & t_{\parallel} f_{\mathbf{k}}^* & 0 & t_3 g_{\mathbf{k}}^* \\ t_{\parallel} f_{\mathbf{k}} & D & t_{\perp} & 0 \\ 0 & t_{\perp} & -D & t_{\parallel} f_{\mathbf{k}}^* \\ t_3 g_{\mathbf{k}} & 0 & t_{\parallel} f_{\mathbf{k}} & -D \end{pmatrix}, \quad (1)$$

where $f_{\mathbf{k}} = 1 + e^{-i\mathbf{k}\cdot\mathbf{a}_1} + e^{-i\mathbf{k}\cdot\mathbf{a}_2}$ and $g_{\mathbf{k}} = e^{-i\mathbf{k}\cdot\mathbf{a}_1} +$

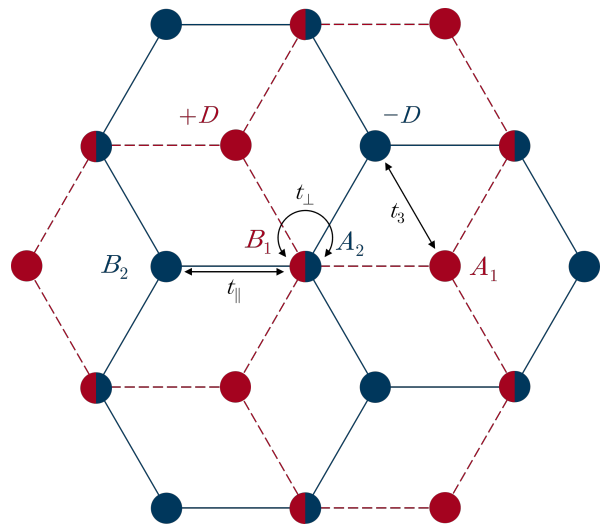


FIG. 1. Bernal bilayer graphene lattice. The A_1 and B_1 atoms (red) are in the top layer ($l = 1$), while the A_2 and B_2 atoms (blue) are in the bottom layer ($l = 2$). The dominant hopping processes t_{\parallel} , t_{\perp} , and t_3 in Eq. (1) are indicated. Due to strong t_{\perp} between overlapping A_2 and B_1 sites, A_1 and B_2 orbitals form the low-energy bands near half-filling.

$e^{-i\mathbf{k}\cdot\mathbf{a}_2} + e^{-i\mathbf{k}\cdot(\mathbf{a}_1+\mathbf{a}_2)}$. Here, $\mathbf{a}_1 = a_0(3\hat{x} + \sqrt{3}\hat{y})/2$ and $\mathbf{a}_2 = a_0(3\hat{x} - \sqrt{3}\hat{y})/2$ are the primitive translation vectors. Typical strengths for the hopping parameters are $t_{\parallel} = 3.3$ eV, $t_{\perp} = 0.42$ eV, and $t_3 = 0.315$ eV [51], which will be used throughout the paper. The eigenvalues are

$$\pm E_{\mathbf{k}}^{\pm} = \pm \sqrt{\left(t_{\parallel}^2 + \frac{t_3^2}{2}\right) |f_{\mathbf{k}}|^2 + D^2 + \frac{t_{\perp}^2}{2} \pm \epsilon_{\mathbf{k}}^2}, \quad (2)$$

where

$$\epsilon_{\mathbf{k}} = \left[\left(t_{\parallel}^2 + \frac{t_3^2}{4}\right) |f_{\mathbf{k}}|^4 t_3^2 + \left((4D^2 + t_{\perp}^2) t_{\parallel}^2 - \frac{t_3^2 t_{\perp}^2}{2}\right) |f_{\mathbf{k}}|^2 + t_{\perp} t_3 t_{\parallel}^2 \left(g_{\mathbf{k}}^* f_{\mathbf{k}}^2 + g_{\mathbf{k}} (f_{\mathbf{k}}^*)^2\right) + \frac{t_{\perp}^4}{4} \right]^{1/4}. \quad (3)$$

The broken-symmetry phases arise near half-filling in the biased BBG system. In this regime, the low-energy bands are located near the Brillouin-zone corners at \mathbf{K} and \mathbf{K}' . In our coordinate system, \mathbf{K} and $\mathbf{K}' = -\mathbf{K}$ are found along $k_x = 0$ at $\mathbf{k} = (0, \pm 4\pi/3\sqrt{3}a_0)$. Fig. 2 displays the four electronic bands $E^{(i)}$, with $i = 1, \dots, 4$ labelled in order of increasing energy about the K points. The displacement field D gaps out the electronic spectrum, resulting in extremely flat bands at certain field strengths [52–55]. The displacement field also polarizes the electronic wavefunctions to just one of the two BBG layers, allowing for tunable proximity effects [56, 57].

The outermost bands $E^{(4)}$ and $E^{(1)}$ with energy $\pm E_{\mathbf{k}}^{\pm}$ arise from symmetric and antisymmetric combinations of the overlapping A_2 and B_1 dimer sites, which are hybridized by t_{\perp} and pushed away from charge neutrality, as shown in Fig. 2. Thus, the low-energy physics are

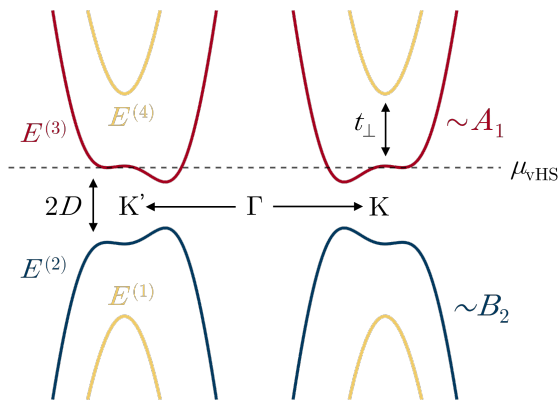


FIG. 2. Low-energy band structure of biased BBG near K and K' . The red and blue bands ($E^{(3)}$ and $E^{(2)}$) originate predominantly from the A_1 and B_2 orbitals, respectively. These bands are gapped out by the displacement field D . The yellow bands ($E^{(4)}$ and $E^{(1)}$) originate from symmetric and antisymmetric combinations of the A_2 and B_1 dimer orbitals, and are pushed away from charge neutrality by the interlayer hopping t_\perp (not to scale). The chemical potential μ is shown tuned to the van Hove singularity within $E^{(3)}$.

dominated by the innermost bands $E^{(3)}$ and $E^{(2)}$, which have energy $\pm E_{\mathbf{k}}^-$, respectively. As has been observed previously [58, 59], these bands originate primarily from the isolated (non-dimer) A_1 and B_2 orbitals. Specifically, the $E^{(2)}$ band (blue) is composed almost exclusively of contributions from the B_2 orbitals. Similarly, the $E^{(3)}$ band (red) is composed primarily of contributions from the A_1 orbitals. Roughly speaking, if we denote by $c_{\mathbf{k}}$ the eigenvector associated with the $E^{(3)}$ band, $c_{\mathbf{k}} \sim \alpha_{\mathbf{k}} a_{1,\mathbf{k}} + \beta_{\mathbf{k}} b_{2,\mathbf{k}}$, where $|\alpha_{\mathbf{k}}| \rightarrow 1$ and $|\beta_{\mathbf{k}}| \rightarrow 0$ as $\mathbf{k} \rightarrow \pm \mathbf{K}$. A similar parameterization holds for the $E^{(2)}$ band. In this way, excess charges above neutrality are localized to layer $l = 1$ [48, 52].

Although we use the full dispersion for the purposes of our mean-field calculations, it is instructive to examine the Taylor expansion of the low-energy bands in the vicinity of \mathbf{K} and \mathbf{K}' . To fourth order in \mathbf{k} ,

$$E_{\mathbf{k}}^- \approx D + u(k_x^2 + k_y^2) + w(k_x^2 + k_y^2)^2 \pm v(k_y^2 - 3k_x^2)k_y, \quad (4)$$

where the plus and minus signs correspond to the K and K' valleys, respectively. $E_{\mathbf{k}}^-$ can be simplified by collecting the symmetric and antisymmetric contributions $\varepsilon_{\mathbf{k}}^s \equiv D + u(k_x^2 + k_y^2) + w(k_x^2 + k_y^2)^2$ and $\varepsilon_{\mathbf{k}}^a \equiv v(k_y^2 - 3k_x^2)k_y$. Introducing the valley index $\tau = \{+, -\}$, we have $E_{\mathbf{k}}^- \approx \varepsilon_{\mathbf{k}}^s + \tau \varepsilon_{\mathbf{k}}^a$ near \mathbf{K} or \mathbf{K}' . The factors u, v , and w are constant functions of the hopping parameters and the displacement field D . The quartic terms are necessary to capture the main features of the full dispersion. $\varepsilon_{\mathbf{k}}^s$ transforms according to the A_1 irreducible representation of C_{3v} , while $\varepsilon_{\mathbf{k}}^a$ transforms according to A_2 . The inversion symmetry is preserved in this expansion, but is now represented as valley exchange $\tau \rightarrow -\tau$ combined

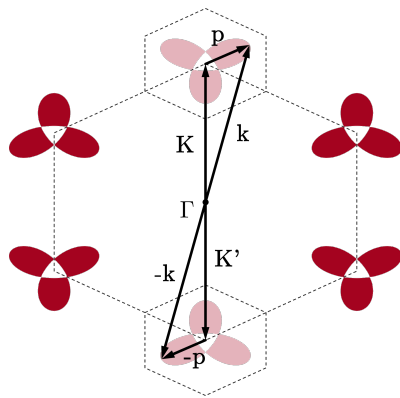


FIG. 3. Low-energy patch description near the valleys. Red trefoils are low-energy Fermi surfaces at the van Hove singularity for $D = 50$ meV (not to scale). The larger hexagon indicates the boundary of the first Brillouin zone. The smaller hexagons represent the momentum-space patches of our low-energy theory (also not to scale). \mathbf{k} is measured from the BZ centre, while $\mathbf{p} = \mathbf{k} - \mathbf{K}$ is measured relative to the \mathbf{K} point.

with $\mathbf{k} \rightarrow -\mathbf{k}$. For $D/t_\perp \ll 1$, the coefficient v is proportional to the trigonal warping t_3 , effectively quantifying the degree of asymmetry.

The van Hove singularities originate from the trigonal warping t_3 and correspond to saddle points in the electronic structure [60]. Each valley possesses three saddle points, one of which is located along the $k_x = 0$ axis. The others are related by a C_3 rotation. At the vHS energy μ_{vHS} , the Fermi surface is a trefoil, as shown in Fig. 3. The saddle points are found at the trefoil vertices. The vHS coordinates can be computed numerically from the full dispersion Eq. (2) by evaluating the Hessian at the extrema, or approximately (but analytically) from the expansion in Eq. (4).

When the system is lightly electron-doped, it is reasonable to limit the single-particle theory to those bands originating from the A_1 sites (band $E^{(3)} \equiv E_{\mathbf{k}}^-$). Introducing the spinor $\Psi_{\mathbf{p},\sigma} = (c_{+,\mathbf{p},\sigma}, c_{-,\mathbf{p},\sigma})^T$, where $\tau \in \{+, -\}$ denotes the valley, $\sigma \in \{\uparrow, \downarrow\}$ denotes spin, and \mathbf{p} is measured from \mathbf{K} or \mathbf{K}' (see Fig. 3), the effective kinetic Hamiltonian near the valleys can be expressed as

$$\mathcal{H}_0 = \sum_{\mathbf{p},\sigma} \Psi_{\mathbf{p},\sigma}^\dagger (\xi_{\mathbf{p}} \tau_0 + \varepsilon_{\mathbf{p}}^a \tau_z) \Psi_{\mathbf{p},\sigma}. \quad (5)$$

Here, $\vec{\tau}$ is a Pauli matrix acting in the valley degree of freedom and we have absorbed the chemical potential μ into $\xi_{\mathbf{p}} \equiv \varepsilon_{\mathbf{p}}^s - \mu$. The momentum \mathbf{p} is restricted to $|\mathbf{p}| \ll |\mathbf{K}|$, as $|\mathbf{K}|$ is the separation between the valleys.

By discarding the high-energy bands, we effectively eliminate the A_2 and B_1 dimer sites. The remaining A_1 and B_2 sites form an emergent honeycomb lattice connected by t_3 . This system closely resembles monolayer graphene with a staggered sublattice potential [61, 62], where here the displacement field plays the role of the staggered potential. Such models are also applicable to WSe_2 and other transition-metal dichalcogenides [63].

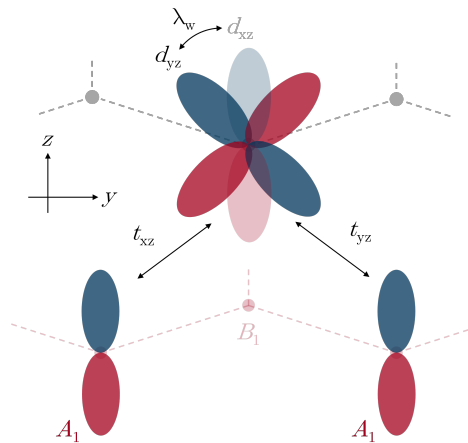


FIG. 4. Schematic depiction of the $A_1 \rightarrow d_{xz/yz} \rightarrow A_1$ (graphene \rightarrow tungsten \rightarrow graphene) hopping processes. The WSe₂ is placed above the BBG, proximate to layer $l = 1$. Electrons from the graphene A_1 p_z -orbitals hop between themselves via an intermediate hopping to the tungsten $d_{xz/yz}$ orbitals, who are mixed by the atomic SOC λ_w . Red and blue colouring of the orbitals correspond to the sign of the wavefunction.

B. Proximity-induced spin-orbit coupling

We now place the BBG on a substrate of monolayer tungsten diselenide, i.e. above the top layer $l = 1$. The heavy tungsten atoms introduce a sizeable atomic spin-orbit coupling term $\mathcal{H}_w = -\lambda_w \mathbf{L} \cdot \mathbf{S}$ to the tungsten d -orbitals of the WSe₂ lattice. Through a second-order hopping process, we show how electrons in the proximate graphene layer inherit Ising SOC. We do not attempt a rigorous derivation, but rather seek a qualitative understanding of its origin.

Due to the trigonal-prismatic crystal-field splitting, the d -orbitals separate into three levels: d_{xz}/d_{yz} , $d_{xy}/d_{x^2-y^2}$, and d_{z^2} [64, 65]. We assume that the active orbitals are the d_{xz}/d_{yz} level, but a similar argument holds if we consider $d_{xy}/d_{x^2-y^2}$ orbitals as the active level. In the subspace spanned by d_{xz} and d_{yz} , $\mathbf{L} \cdot \mathbf{S}$ behaves like $L_z S_z$ and we have explicitly $L_z S_z |xz, \sigma\rangle = i\sigma |yz, \sigma\rangle$ and $L_z S_z |yz, \sigma\rangle = -i\sigma |xz, \sigma\rangle$. The S_z operator is even under spatial inversion but L_z changes sign. As the two graphene valleys are related by inversion, the effective SOC interaction has opposite sign for \mathbf{K} and \mathbf{K}' resulting in a τ_z dependence.

To see how this comes about, we consider a simplified model of the BBG-WSe₂ heterostructure. We take as our starting point the triangular sublattice of the A_1 sites. Focusing on momentum $\mathbf{K} = (0, K_y)$, we consider a hopping process involving the p_z -orbitals of A_1 and the d -orbitals of tungsten along the y -axis (see Fig. 4).

Imagine an A_1 electron hops to a d_{xz} orbital, whereupon it is mixed with d_{yz} by the atomic SOC λ_w , and then hops back to A_1 . Such process leads to the effective

SOC term

$$\mathcal{H}_\lambda \sim \frac{t_{xz} \lambda_w t_{yz}}{E_{pd}^2} \sigma \delta_{\sigma\sigma'}, \quad (6)$$

where the standard perturbation theory has been employed assuming that E_{pd} , the atomic energy difference between p_z and d_{xz}/d_{yz} is much larger than λ_w , t_{xz} , and t_{yz} . The t_{yz} hopping changes sign under $y \rightarrow -y$, but t_{xz} does not (see Fig. 4). Thus, from Eq. (6) it becomes clear that the SOC interaction takes opposite sign in opposite valleys (i.e. under $K_y \rightarrow -K_y$). Note that the tungsten atoms must be displaced slightly along the x -direction to allow for finite t_{xz} , which would otherwise be zero by symmetry.

Introducing $\Psi_{\mathbf{p}} = (c_{+, \mathbf{p}, \uparrow}, c_{-, \mathbf{p}, \uparrow}, c_{+, \mathbf{p}, \downarrow}, c_{-, \mathbf{p}, \downarrow})^T$, the effective Ising SOC Hamiltonian acting in the A_1 subspace reduces to

$$\mathcal{H}_\lambda = \lambda \sum_{\mathbf{p}} \Psi_{\mathbf{p}}^\dagger (\sigma_z \tau_z) \Psi_{\mathbf{p}}, \quad (7)$$

where $\vec{\sigma}$ is another Pauli matrix acting in the spin degree of freedom and $\lambda \sim t_{xz} \lambda_w t_{yz} / E_{pd}^2$. Within our patch model, the SOC strength is approximated as constant in magnitude, with equal and opposite values in the \mathbf{K} and \mathbf{K}' valleys. The constant-magnitude approximation is reasonable, as the Fermi surface pockets are small. For the same reason, we neglect Rashba SOC. The effective low-energy single-particle Hamiltonian is then given by $\mathcal{H}_0 + \mathcal{H}_\lambda$.

Our simplified treatment does not take into account the lattice geometry of the WSe₂/BBG heterostructure. In particular, due to the lattice mismatch between the graphene and the WSe₂, the hopping process described above may only be possible in certain domains of the sample. However, even with a relative twist angle between the lattices, Ising SOC is expected to be generic; only the magnitude of λ is affected by twist angle [11]. A more sophisticated study taking into account the atomic sites of the supercell using first-principle methods reported an effective Ising SOC near the K points consistent with the above result [66, 67]. Another microscopic model for the origin of Ising SOC is proposed in Ref. [59].

C. Fermi surface topology

It is useful to establish how the Fermi surface (FS) changes in the presence of SOC. In Fig. 5, we present the FS topology for the tight-binding model as a function of the chemical potential μ , for three choices of the SOC strength λ . We focus on electron-doping into the $E^{(3)}$ band. Our results apply equally for hole-doping into the $E^{(2)}$ band due to particle-hole symmetry.

In the absence of SOC, the system possesses four degenerate bands (spin \times valley). There is a vHS at $\mu_{\text{vHS}} \approx D$ (here we take $D = 50$ meV). As the chemical potential moves through the vHS, each of the four degenerate Fermi surfaces separate into three Fermi pockets.

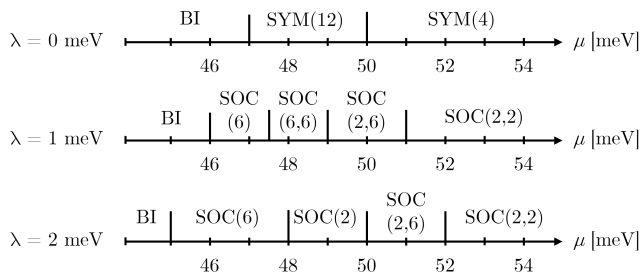


FIG. 5. Evolution of Fermi surface (FS) topology for the effective tight binding model $\mathcal{H}_0 + \mathcal{H}_\lambda$ as a function of μ for three different values of λ . The vertical lines indicate a transition in the FS topology. SYM and SOC refers to the symmetric band without SOC and to the band with SOC, respectively. The index inside the bracket counts the number of FS pockets. When there are two different sized pockets, two indices are used for large and small pockets. BI stands band insulator. We set $D = 50$ meV.

As μ increases, the FS topology changes from SYM(12) to SYM(4). Here, ‘SYM’ indicates a FS topology without any broken symmetry, and the index counts the number of equal-sized FS pockets. For chemical potentials below the band edge, the system is a simple band insulator (BI).

When $\lambda \neq 0$, the four-fold degeneracy is lowered to two sets of two-fold degenerate bands. The two-fold degenerate vHSs occur at $\mu \approx D \pm \lambda$. The SOC thus allows for various other FS topologies. In Fig. 5, ‘SOC’ refers to the bands with finite λ and the two indices (α, β) count the number of unequal-sized FS pockets in order of decreasing size. For example, SOC(2,6) labels the topology consisting of 2 larger and 6 smaller Fermi pockets. Some topologies such as SOC(6,6) and SOC(2) are only available for $2\lambda < W$ and $2\lambda > W$, respectively, where $W \approx 3.4$ meV is the bandwidth between the band edge and the local band minimum.

III. LOW-ENERGY EFFECTIVE INTERACTION HAMILTONIAN

Now that we have established the low-energy tight-binding model $\mathcal{H}_0 + \mathcal{H}_\lambda$, including the Ising SOC, we turn to the low-energy interactions of doped electrons near the valleys to capture the possible broken-symmetry states. The interacting Hamiltonian for electrons on the non-dimer A_1 and B_2 sites, including on-site, NN, and NNN Hubbard interactions, is given by

$$\begin{aligned} \mathcal{H}_{\text{int}} = & U_{A_1} \sum_{i \in A_1} n_{i,\uparrow} n_{i,\downarrow} + U_{B_2} \sum_{i \in B_2} n_{i,\uparrow} n_{i,\downarrow} \\ & + V_0 \sum_{\langle i,j \rangle} n_i n_j + V'_0 \sum_{\langle\langle i,j \rangle\rangle} n_i n_j, \end{aligned} \quad (8)$$

where $n_{i \in A_1} = \sum_{\sigma} a_{1,i,\sigma}^\dagger a_{1,i,\sigma}$ is the electron density operator for A_1 sites, and similarly $n_{j \in B_2} = \sum_{\sigma} b_{2,j,\sigma}^\dagger b_{2,j,\sigma}$

for B_2 sites. Here, U_{A_1} and U_{B_2} are the on-site Hubbard interactions at A_1 and B_2 , respectively. V_0 is the NN density-density interaction between electrons on A_1 and B_2 which form the emergent honeycomb lattice. V'_0 is the NNN interaction between A_1 and A_1 or B_2 and B_2 . All interactions are assumed repulsive.

At half-filling, the low-energy triangular B_2 sublattice is fully occupied due to the displacement field D . When the system is lightly electron-doped, the additional electrons are constrained to the high-energy A_1 sublattice. The effective interacting Hamiltonian for A_1 electrons can be derived using a Schrieffer-Wolff transformation, similar to the procedure carried out in Ref. [47] for a honeycomb lattice with a staggered sublattice potential.

Including occupations of up to three fermions per upper triangle, the resulting low-energy interacting Hamiltonian is found to be

$$\begin{aligned} \mathcal{H}_{\text{int}}^{\text{eff}} = & \sum_{\langle i,j \rangle, \sigma} \left[\frac{\tilde{t}}{2} (n_i + n_j) \right] \left(a_{1,i,\sigma}^\dagger a_{1,j,\sigma} + h.c. \right) \\ & + \gamma \sum_{ijk \in \Delta, \sigma} \left(a_{1,i,\sigma}^\dagger n_k a_{1,j,\sigma} + P_{ijk} \right) \\ & + U \sum_i n_{i\uparrow} n_{i\downarrow} + V \sum_{ij} n_i n_j, \end{aligned} \quad (9)$$

where $\bar{D} = 2D - U_{A_1} + 3V_0 - 12V'_0$, $\gamma = t_0^2/(\bar{D} + 2V'_0) - t_0^2/(\bar{D} + V_0) > 0$, and $\tilde{t} = t_0^2/(\bar{D} + 2V'_0) + t_0^2/(\bar{D} + U_{A_1} + 3V'_0) - 2t_0^2/(\bar{D} + V_0) > 0$. Here, t_0 is the effective bandwidth of band $E_{\mathbf{k}}^{(3)}$ near the valley. The renormalized interactions go as $U \sim U_{A_1}$ and $V \sim V'_0$, assuming that $D \gg U_{A_1} > V_0 > 2V'_0 > t_0$. The interaction $\gamma \rightarrow 0$ as $V_0, V'_0 \rightarrow 0$, and corresponds to correlated hopping between three sites of $i, j, k \in A_1$ due to the presence of occupied B_2 sites in the middle of a triangle formed by NN A_1 atoms (P_{ijk} refers to permutation among the ijk forming the triangle). Note that we have not included the Ising SOC λ in this procedure as $\lambda \ll (D, t)$.

Focusing on momenta near the valleys $\tau \in \{+, -\}$, and retaining fermionic modes $a_{1,\tau K+\mathbf{p},\sigma} \equiv c_{\tau,\mathbf{p},\sigma}$, a Fourier transform of the above model results in

$$\mathcal{H}_{\text{int}}^{\text{eff}} = \frac{1}{N} \sum_{\mathbf{q}} g_1 \rho_+(\mathbf{q}) \rho_-(-\mathbf{q}) + g_2 \mathbf{s}_+(\mathbf{q}) \cdot \mathbf{s}_-(-\mathbf{q}), \quad (10)$$

where

$$\rho_\tau(\mathbf{q}) \equiv \sum_{\mathbf{p}, \sigma} c_{\tau,\mathbf{p},\sigma}^\dagger c_{\tau,\mathbf{p}+\mathbf{q},\sigma} \quad (11)$$

and

$$\mathbf{s}_\tau(\mathbf{q}) \equiv \frac{1}{2} \sum_{\sigma\sigma'} \sum_{\mathbf{p}} c_{\tau,\mathbf{p},\sigma}^\dagger \boldsymbol{\sigma}_{\sigma\sigma'} c_{\tau,\mathbf{p}+\mathbf{q},\sigma'}. \quad (12)$$

The parameters g_1 and g_2 are given by

$$\begin{aligned} g_1 &= \frac{1}{2} (U + 15V - 24\gamma - 6\tilde{t}) > 0, \\ g_2 &= -2(U - 3V + 12\gamma - 6\tilde{t}) < 0. \end{aligned} \quad (13)$$

As we will discuss in Sec. VI, the WSe₂ substrate may modify the strengths of g_1 and g_2 in addition to inducing the Ising SOC. Below we consider a full Hamiltonian $\mathcal{H}_0 + \mathcal{H}_\lambda + \mathcal{H}_{\text{int}}$ and explore possible broken-symmetry states within MF theory. We limit our study to broken-symmetry states with zero centre-of-mass momentum $\mathbf{q} = 0$.

IV. MEAN-FIELD ORDER PARAMETERS

Note that g_1 is repulsive while g_2 is attractive, indicating that they act like the density-density and Hund's coupling between the valleys. Let us examine the attractive channels. Since the interactions can be reformulated as $-g_1(\rho_+ - \rho_-)^2$ and $g_2(\mathbf{s}_+ + \mathbf{s}_-)^2$, with $g_1 > 0$ and $g_2 < 0$, they lead to attractive channels for valley polarization (P_z) and spin polarization (\mathbf{M}) with $\mathbf{q} = 0$:

$$P_z \equiv \frac{1}{2} \langle (\rho_+ - \rho_-) \rangle, \quad \mathbf{M} \equiv \langle (\mathbf{s}_+ + \mathbf{s}_-) \rangle. \quad (14)$$

Intervalley-order parameters P_x and P_y are also possible. We collect the three isospin components into a vector

$$\mathbf{P} = \frac{1}{2} \sum_{\tau\tau', \mathbf{p}, \sigma} \langle (c_{\tau, \mathbf{p}, \sigma}^\dagger (\boldsymbol{\tau})_{\tau\tau'} c_{\tau', \mathbf{p}, \sigma}) \rangle. \quad (15)$$

Given the trigonal warping associated with the $\varepsilon_{\mathbf{p}}^a \tau_z$ term in Eq. (5), we expect P_z to be different from P_x and P_y . Spin and valley polarization are treated on equal footing, in that spin polarization is valley-independent and valley polarization is spin-independent.

We also consider the particle-particle channel. The MF interaction strength for the spin-singlet is $(g_1 - \frac{3}{4}g_2)/2 > 0$, i.e. repulsive due to $g_1 > 0$ and $g_2 < 0$. For this reason we do not expect the spin-singlet to form. However, the spin-triplet has an attractive interaction [47] and is associated with the order parameter

$$\Delta = \frac{1}{2} \sum_{\tau\tau', \mathbf{p}, \sigma\sigma'} \langle c_{\tau, \mathbf{p}, \sigma} (i\sigma_y \boldsymbol{\sigma} \cdot \hat{d})_{\sigma\sigma'} (i\tau_y)_{\tau\tau'} c_{\tau', -\mathbf{p}, \sigma'} \rangle. \quad (16)$$

Here, \hat{d} denotes the d -vector, which is perpendicular to the spin of the Cooper-pair condensate, i.e. $\hat{d} \cdot \mathbf{S} |\psi_{sc}\rangle = 0$, where \mathbf{S} is the total spin of the Cooper pair and $|\psi_{sc}\rangle$ is a spin-triplet SC state. For example, when $\hat{d} = \hat{z}$, the triplet occurs in $S_z = 0$. Note that the above spin triplet is a valley-singlet SC, and thus the antisymmetric wave function condition is satisfied under the exchange of the two valleys.

The interacting MF Hamiltonian can be recast as

$$\begin{aligned} \mathcal{H}_{\text{int}}^{\text{MF}} = & V_P \sum_{\tau\tau', \mathbf{p}, \sigma} c_{\tau, \mathbf{p}, \sigma}^\dagger (\boldsymbol{\tau} \cdot \mathbf{P})_{\tau\tau'} c_{\tau', \mathbf{p}, \sigma} \\ & + V_M \sum_{\tau, \mathbf{p}, \sigma\sigma'} c_{\tau, \mathbf{p}, \sigma}^\dagger (\boldsymbol{\sigma} \cdot \mathbf{M})_{\sigma\sigma'} c_{\tau, \mathbf{p}, \sigma'} \\ & + \frac{V_T}{2} \sum_{\tau\tau', \mathbf{p}, \sigma\sigma'} c_{\tau, \mathbf{p}, \sigma}^\dagger (\vec{\Delta} \cdot \boldsymbol{\sigma} i\sigma_y)_{\sigma\sigma'} (i\tau_y)_{\tau\tau'} c_{\tau', -\mathbf{p}, \sigma'}, \end{aligned} \quad (17)$$

where the MF interaction strengths are given by

$$\begin{aligned} V_P &= -g_1, \\ V_M &= \frac{1}{4}g_2, \\ V_T &= \frac{1}{2} \left(g_1 + \frac{1}{4}g_2 \right). \end{aligned} \quad (18)$$

The attractive interaction is obtained for the spin triplet when $-g_2 > 4g_1$. Rewriting g_1 and g_2 in terms of \tilde{t} , γ , U , and V [Eq. (13)], we have $2V_T = 9V - 18\gamma$, indicating that the attractive interaction for the SC originates from γ , the assisted hopping interaction. Meanwhile, for the spin- and valley-polarizing channels, we obtain attractive interactions for any $g_1 > 0$ and $g_2 < 0$. Solving for the order parameters, \mathbf{P} , \mathbf{M} , and Δ self-consistently at zero temperature, we obtain the MF results presented in the next section.

V. MEAN-FIELD RESULTS AND IMPLICATIONS

In this section, we first present our MF results as a function of μ for three choices of (g_1, g_2) , with and without SOC. The full phase diagrams will be discussed later. In Fig. 6, the left column shows the results for $\lambda = 0$ and the right column for $\lambda = 2$ meV. From top to bottom, $|g_2|/g_1$ increases. More specifically, the interactions are parameterized by $g_1 = g \cos(\theta)$, $g_2/4 = -g \sin(\theta)$. In this way, $\theta = \pi/4$ corresponds $|g_2/4g_1| = 1$ where $|V_P|/|V_M| = 1$ and V_T becomes attractive. Panels (a), (b), and (c) correspond to $\theta = \pi/10, 5\pi/16$, and $2\pi/5$, respectively. These θ correspond (roughly) to $(g_1, g_2/4) = (6.7, -2.2)$, $(3.9, -5.8)$, and $(2.2, -6.7)$ meV.

A. Effects of interactions without Ising SOC

As is evident from the MF Hamiltonian in Eq. (17), the interaction parameter g_1 favours valley polarization (VP) and intervalley order (IVO), characterized by finite P_z and (P_x, P_y) , respectively. The attractive g_2 favours spin polarization (SP) and spin-triplet superconductivity (SC). When $\lambda = 0$ (left panel in Fig. 6), the vHS is located around $\mu_{\text{vHS}} \approx 50$ meV. The IVO, VP, SP, and SPSC (SP coexisting with SC) phases emerge near the vHS as the ratio $|g_2|/g_1$ increases from top to bottom.

Let us first consider case (a), where VP and IVO occur due to V_P dominating over V_M and V_T , with V_T being repulsive. The abrupt onset of the VP order parameter as the chemical potential approaches the vHS indicates a first-order transition resembling the Pomeranchuk (or nematic) instability. The density difference between valleys leads to a splitting of the vHS into two distinct vHSs (one below and one above μ_{vHS}), thereby lowering the system's energy [68, 69]. There is a first-order transition to IVO, developing when the chemical potential is tuned

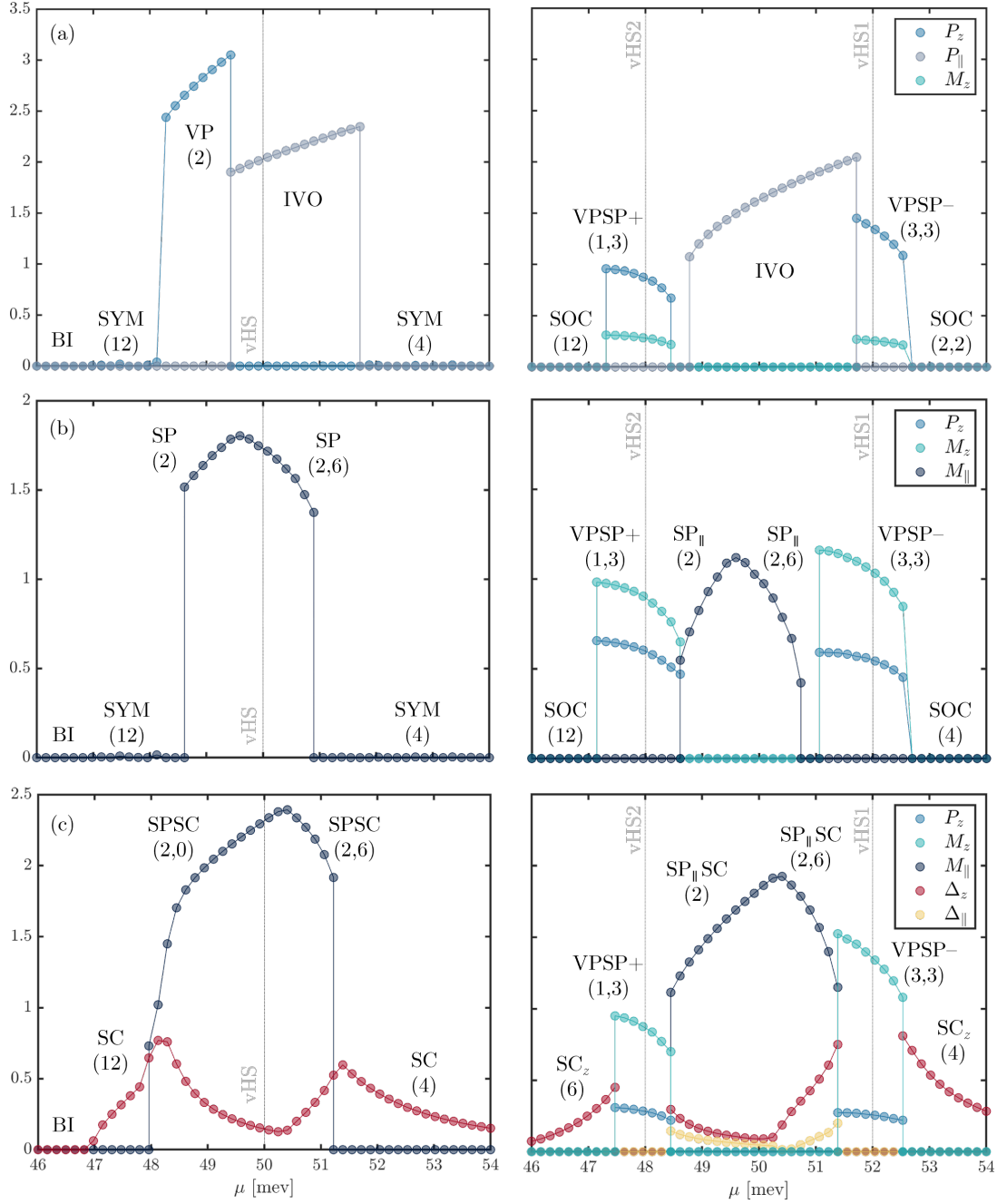


FIG. 6. Order parameter amplitudes (in unit of meV) as a function of μ for three different sets of (g_1, g_2) . IVO, VP, SP, VPSP, SC, and SPSC refer to intervalley-ordered, valley-polarized, spin-polarized, valley- and spin-polarized, superconducting, and spin-polarized superconducting states, respectively. Left and right column are for $\lambda = 0$ and $\lambda = 2$ meV, respectively. (a) $g_1 = 6.7$ meV and $g_2 = -8.7$ meV, leading to $V_P = -6.7$ meV, $V_M = -2.2$ meV, and $V_T > 0$. The location of the vHSs are indicated. (b) $g_1 = 3.9$ meV and $g_2 = -23.3$ meV, leading to $V_P = -3.9$ meV and $V_M = -5.8$ meV. V_T is attractive, but spin-triplet SC is absent as the interaction is too weak ($V_T \approx -1$ meV). For the $\lambda = 0$ cases, $M_x = M_y \equiv M_{||} = M_z$ and only $M_{||}$ is shown for clarity. Similarly, $P_x = P_y \equiv P_{||}$ for IVO. (c) $g_1 = 2.2$ meV, $g_2 = -26.6$ meV leading to $V_P = -2.2$ meV, $V_M = -6.7$ meV, and $V_T = -2.2$ meV. The triplet magnitude has been multiplied by a factor of 2 for visibility. These plots are representative linecuts of Fig. 7 at (a) $\theta = \pi/10$, (b) $\theta = 5\pi/16$, and (c) $\theta = 2\pi/5$. From top to bottom, $|g_2|/g_1$ increases.

deeper into the band. A similar transition has been observed in rhomboherdal trilayer graphene [27].

IVO hybridizes the K and K' bands, while VP can only shift them up and down. Hybridization can be energetically favourable if it gaps out the Fermi surface. As discussed above, the $SU(2)$ isospin symmetry of \mathbf{P} is broken by the τ_z -dependence in the electronic dispersion, and the degree of asymmetry is parameterized by the trigonal warping t_3 . At $t_3 = 0$, the $SU(2)$ symmetry is restored and we find the degenerate solution $P_x = P_y = P_z$. For finite t_3 , we find a first-order transition between VP and IVO. The critical μ depends on details of the calculation, namely the strengths of t_3 and V_P .

Moving now to panel (b), as the ratio $|g_2|/g_1$ increases, V_M becomes dominant over V_P and the VP order parameter is replaced by the SP order parameter. Like VP, the SP order parameter also develops around μ_{vHS} . The first-order transition from the symmetric (SYM) state highlights the significance of trigonal warping near the vHS, which differs from the conventional second-order Stoner instability.

Finally, consider case (c), where $|g_2|/4g_1 > 1$ results in an attractive spin-triplet SC interaction. With the chosen values of (g_1, g_2) , the SC order parameter is finite and coexists with SP close to the vHS. In the pure SC regime, the orientation of the d -vector is arbitrary. However, within the coexistence region, the d -vector is pinned to the plane perpendicular to the (spontaneously chosen) magnetization axis. In the SYM state, the SC order parameter develops continuously. However, when the SP state occupies the phase space near μ_{vHS} , the strength of the SC order parameter is suppressed. One might expect the large DOS available at the vHS to enhance superconductivity, however the spontaneous spin splitting pushes the vHS away from the pairing surface, resulting in a suppression of the superconducting gap.

The modification of the FS topologies in the ordered states are labelled in Fig. 6, according to the scheme described in Sec. II. FS topologies for IVO are more complicated, and change rapidly with μ . We acknowledge that order-parameter magnitudes are typically overestimated by MF theory, and so our labelling of the FS topologies in the symmetry-broken phases may differ beyond MF.

B. Effects of Ising SOC

As previously noted, the Ising SOC splits the original vHS at $\mu_{\text{vHS}} \approx D$ into two distinct values at approximately $D \pm \lambda$. We define these as $\mu_{\text{vHS}_1} \equiv D + \lambda$ and $\mu_{\text{vHS}_2} \equiv D - \lambda$, as illustrated by the pair of vertical lines in the right panels of Fig. 6. With this context, let us examine cases (a) through (c) in the presence of finite $\lambda = 2$ meV. Due to the symmetry of the Ising SOC, $M_x = M_y$ and $\Delta_x = \Delta_y$ are degenerate solutions, which we represent by M_{\parallel} and Δ_{\parallel} , respectively.

In case (a), where V_P dominates over V_M and V_T , the finite VP state bifurcates and shifts to regions near the

new vHS locations, μ_{vHS_1} and μ_{vHS_2} . This behaviour suggests that the VP state closely resembles the Pomeranchuk instability associated with the vHS, similar to the $\lambda = 0$ case. Additionally, we observe a finite spin polarization induced by the Ising SOC due to the linear coupling between P_z and M_z through the term $\lambda\tau_z\sigma_z$. Since $\lambda > 0$, naively one expects opposite sign of P_z and M_z in the VPSP phase (denoted by VPSP $-$). This expectation is met near μ_{vHS_1} , but near μ_{vHS_2} the same sign of P_z and M_z (denoted by VPSP $+$) occurs. The explanation has to do with which set of SOC-polarized bands participate in the Pomeranchuk transition. The IVO is less sensitive to the shifted vHSs, and persists in the intermediate region between μ_{vHS_1} and μ_{vHS_2} . In principle, the IVO phase can support superconductivity, but in the superconducting regime V_P is small and IVO does not develop.

In case (b), the strong tendency to develop VP near the vHSs persists, even though V_M dominates over V_P . Near μ_{vHS_1} and μ_{vHS_2} , VP is induced by M_z through the combined effects of Ising SOC and proximity to the vHS. The three components of the magnetization (M_x, M_y, M_z) are inequivalent because of the Ising SOC, which tends to polarize along the z -axis. Similar to case (a), VPSP $-$ and VPSP $+$ occur near μ_{vHS_1} and μ_{vHS_2} , respectively. Conversely, away from the vHS points, the SP state persists without the presence of VP order, but only M_x and M_y are finite (denoted by SP $_{\parallel}$). In this phase, the valley-resolved spin projections are canted, with equal and opposite M_z components for K and K' . The in-plane magnetization are equal in K and K' , resulting in a net in-plane magnetization for the system. The canting angle depends on the relative magnitudes of λ and M_{\parallel} . This phase has been observed in the self-consistent Hartree-Fock calculations of Ref. [31].

The reemergence of VP near the vHSs is also evident in case (c), where the spin-triplet SC coexists with SP in the absence of SOC. When SOC is introduced, the VPSP state emerges near μ_{vHS_1} and μ_{vHS_2} . The presence of VP, which differentiates the FS at the two valleys, strongly suppresses SC. Our analysis indicates that transitions between the VPSP and SC states are first-order, with no coexistence of VP and SC. When the VPSP disappears away from the vHSs, the SC persists. However, when μ is located between the two vHSs, the earlier SP $_{\parallel}$ in case (b) turns into SP $_{\parallel}$ SC with inequivalent Δ_{\parallel} and Δ_z . The Ising SOC favours the Δ_z component because Δ_z pairs opposite spins between opposite valleys with the same size of partner FS. The Δ_{\parallel} component therefore weakens, but is still finite within SP $_{\parallel}$ SC. The pure SC denoted by SC(4) develops for $\mu > \mu_{\text{vHS}_1}$ where only Δ_z is finite, and where the number 4 refers to the number of the underlying FS pockets before the SC gap develops. A second region of spin-unpolarized superconductivity SC(6) with only Δ_z finite develops when $\mu < \mu_{\text{vHS}_2}$, close the band edge of the SOC-split bands. The underlying FS consists of 6 Fermi pockets with opposite spin and opposite valley quantum numbers.

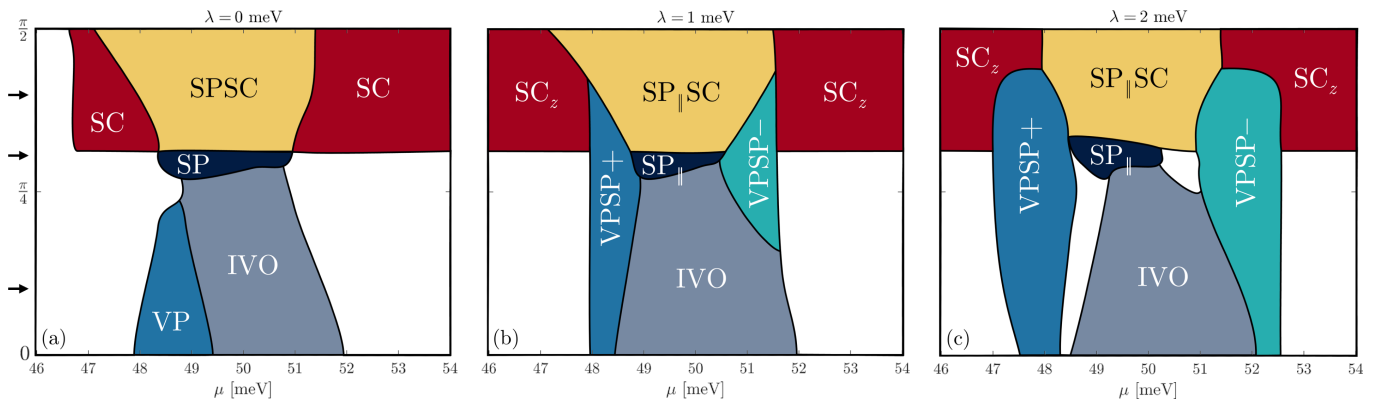


FIG. 7. Phase diagrams as a function of μ and interaction strength for (a) $\lambda = 0$, (b) $\lambda = 1$ meV, and (c) $\lambda = 2$ meV. The interaction strengths are parameterized as $g_1 = g \cos(\theta)$ and $g_2/4 = -g \sin(\theta)$, so that $\theta = \pi/4$ corresponds to $|g_2/4g_1| = 1$, where $|V_P/V_M| = 1$ and V_T becomes attractive. We set $g = 7$ meV. The three arrows indicate the location of the linecuts in Fig. 6. Disordered phases are shown in white.

C. Phase diagram

The overall phase diagram as a function of $|g_2|/g_1$ and μ is shown in Fig. 7 for three different values of λ . As discussed earlier, when the Ising SOC is absent, IVO and VP occur near the vHS and persist roughly until $|g_2| \approx 4g_1$. As $|g_2|$ increases further, IVO transitions into SP, followed by a coexistence of SP and SC (SPSC). Away from the vHS, the spin-triplet SC occurs when $|g_2| > 4g_1$. The appearance of a sharp onset of the SC state as $|g_2|/g_1$ increases is unphysical; the SC order parameter will develop gradually once $|g_2| \sim 4g_1$, except near the top-left corner of (a), where the chemical potential passes through the band edge.

As λ increases from 0 to 1 meV, the VPSP phases emerge near μ_{vHS_1} and μ_{vHS_2} . Interestingly, when $|g_2| \approx 4g_1$, the VPSP phase begins to encroach upon the phase space of both SC and SPSC. A reduction in occupied phase space of SC near the vHS has been observed in Ref. [17]. $\text{SP}_{||}$ is confined to the phase space near $|g_2| \approx 4g_1$ and μ_{vHS} , i.e. in between μ_{vHS_1} and μ_{vHS_2} . The SC region occurring away from the vHSs is not enhanced by the Ising SOC, except for $\mu < \mu_{\text{vHS}_2}$, i.e. in the top-left corner. This is simply a result of the splitting induced by λ , pushing off one set of bands towards lower energies. While the SC phase is not significantly extended by the Ising SOC, the strength of the SC order parameter can be tuned by the SOC by modifying the DOS near the Fermi level. The phase space where the SC gap is largest is found at the phase boundaries of SC and SPSC, even in the absence of SOC. This may help to explain the two distinct SC regions reported in Ref. [24]

As λ is increased up to 2 meV, the VPSP phases overtake more of the phase diagram, encroaching further upon SC and SPSC. In the region near μ_{vHS} , for $|g_2| < 4g_1$, pockets of disordered phases emerge at the phase boundaries. This is because μ_{vHS_1} and μ_{vHS_2} are pushed further apart as λ increases, leaving some densities at very low DOS.

VI. DISCUSSION AND SUMMARY

Motivated by the emergence of superconductivity in biased BBG proximate to WSe₂, we investigate the role of Ising SOC in promoting superconductivity. First, we provide a qualitative description for the possible origin of Ising SOC through hopping between the p -orbitals of graphene and the d -orbitals of tungsten. We then derive an interacting model based on the observation that the low-energy bands of biased BBG resemble those of a honeycomb lattice with a staggered sublattice potential, where spin-triplet superconductivity has been found via momentum-space Hund's coupling [47]. However, the competition between superconductivity with other symmetry-broken phases and their interplay with the van Hove singularity have yet to be explored.

By applying a Schrieffer-Wolff transformation, including further next-nearest-neighbor interactions, we find that valley-singlet spin-triplet superconductivity coexists with magnetic order near the van Hove singularity, when the Hund's coupling (g_2) is sufficiently large. However, for smaller g_2 , the system develops valley polarization or intervalley order, foregoing superconductivity. When Ising SOC is introduced, superconductivity is further suppressed near the van Hove singularities by a competing phase with coexisting valley and magnetic order. The enhancement of superconductivity due to Ising SOC occurs only in a small region of phase space where the enhanced density of states leads to a larger superconducting gap. This requires fine-tuning of the chemical potential. In contrast to other proposals [36, 38, 39, 42], the general behaviour is that Ising SOC promotes coexisting valley and magnetic order near the van Hove singularity, suppressing superconductivity.

Based on the effective interactions derived from the Schrieffer-Wolff transformation, we speculate that the proximate WSe₂ monolayer effectively reduces the repulsive Coulomb interaction among doped electrons $V \sim V'_0$, which in turn weakens the attractive interactions re-

sponsible for valley and magnetic orders while enhancing those that promote superconductivity. To test this hypothesis, we propose a heterostructure of BBG with lighter 3d transition-metal monolayers that have weaker atomic SOC, to observe if superconductivity emerges. While hydrostatic pressure could enhance screening, it also increases the Ising SOC itself [16], making it difficult to disentangle the two effects. Future theoretical and experimental studies are needed to understand the enhancement of superconductivity in BBG heterostructures with strong Ising SOC.

ACKNOWLEDGMENTS

This work was supported by the Natural Sciences and Engineering Research Council of Canada (NSERC) Dis-

covery Grant No. 2022-04601 and the Canadian institute for Advanced Research. H.Y.K acknowledges support from the Canada Research Chairs Program and the Simons Emmy Noether fellowship program of the Perimeter Institute, supported by a grant from the Simons Foundation (1034867, Dittrich). Computations were performed on the Niagara supercomputer at the SciNet HPC Consortium. SciNet is funded by: the Canada Foundation for Innovation under the auspices of Compute Canada; the Government of Ontario; Ontario Research Fund - Research Excellence; and the University of Toronto.

-
- [1] Y. Cao, V. Fatemi, S. Fang, K. Watanabe, T. Taniguchi, E. Kaxiras, and P. Jarillo-Herrero, *Nature (London)* **556**, 43 (2018), arXiv:1803.02342 [cond-mat.mes-hall].
- [2] R. Bistritzer and A. H. MacDonald, *Proceedings of the National Academy of Science* **108**, 12233 (2011), arXiv:1009.4203 [cond-mat.mes-hall].
- [3] E. Y. Andrei and A. H. MacDonald, *Nature Materials* **19**, 1265 (2020), arXiv:2008.08129 [cond-mat.mes-hall].
- [4] H. Zhou, L. Holleis, Y. Saito, L. Cohen, W. Huynh, C. L. Patterson, F. Yang, T. Taniguchi, K. Watanabe, and A. F. Young, *Science* **375**, 774 (2022), arXiv:2110.11317 [cond-mat.mes-hall].
- [5] S. C. de la Barrera, S. Aronson, Z. Zheng, K. Watanabe, T. Taniguchi, Q. Ma, P. Jarillo-Herrero, and R. Ashoori, *Nature Physics* **18**, 771 (2022), arXiv:2110.13907 [cond-mat.mes-hall].
- [6] Y. Zhang, R. Polski, A. Thomson, É. Lantagne-Hurtubise, C. Lewandowski, H. Zhou, K. Watanabe, T. Taniguchi, J. Alicea, and S. Nadj-Perge, *Nature (London)* **613**, 268 (2023), arXiv:2205.05087 [cond-mat.supr-con].
- [7] H. Min, J. E. Hill, N. A. Sinitsyn, B. R. Sahu, L. Kleinman, and A. H. MacDonald, *Phys. Rev. B* **74**, 165310 (2006), arXiv:cond-mat/0606504 [cond-mat.mes-hall].
- [8] S. Konschuh, M. Gmitra, and J. Fabian, *Phys. Rev. B* **82**, 245412 (2010).
- [9] S. Konschuh, M. Gmitra, D. Kochan, and J. Fabian, *Phys. Rev. B* **85**, 115423 (2012), arXiv:1111.7223 [cond-mat.mes-hall].
- [10] J. Sichau, M. Prada, T. Anlauf, T. J. Lyon, B. Bosnjak, L. Tiemann, and R. H. Blick, *Phys. Rev. Lett.* **122**, 046403 (2019).
- [11] A. David, P. Rakyta, A. Kormányos, and G. Burkard, *Phys. Rev. B* **100**, 085412 (2019), arXiv:1905.08688 [cond-mat.mes-hall].
- [12] M. Gmitra and J. Fabian, *Phys. Rev. Lett.* **119**, 146401 (2017).
- [13] Z. Wang, D.-K. Ki, H. Chen, H. Berger, A. H. MacDonald, and A. F. Morpurgo, *Nature Communications* **6**, 8339 (2015), arXiv:1508.02912 [cond-mat.mes-hall].
- [14] Z. Wang, D.-K. Ki, J. Y. Khoo, D. Mauro, H. Berger, L. S. Levitov, and A. F. Morpurgo, *Physical Review X* **6**, 041020 (2016), arXiv:1606.01789 [cond-mat.mes-hall].
- [15] D. Wang, S. Che, G. Cao, R. Lyu, K. Watanabe, T. Taniguchi, C. N. Lau, and M. Bockrath, *Nano Letters* **19**, 7028 (2019), arXiv:1909.10931 [cond-mat.mes-hall].
- [16] B. Szentpéteri, A. Márffy, M. Kedves, E. Tóvári, B. Fülöp, I. Kükemezey, A. Magyarkuti, K. Watanabe, T. Taniguchi, S. Csonka, and P. Makk, *arXiv e-prints*, arXiv:2409.20062 (2024), arXiv:2409.20062 [cond-mat.mes-hall].
- [17] Y. Zhang, G. Shavit, H. Ma, Y. Han, K. Watanabe, T. Taniguchi, D. Hsieh, C. Lewandowski, F. von Oppen, Y. Oreg, and S. Nadj-Perge, *arXiv e-prints*, arXiv:2408.10335 (2024), arXiv:2408.10335 [cond-mat.supr-con].
- [18] A. M. Seiler, F. R. Geisenhof, F. Winterer, K. Watanabe, T. Taniguchi, T. Xu, F. Zhang, and R. T. Weitz, *Nature (London)* **608**, 298 (2022), arXiv:2111.06413 [cond-mat.mes-hall].
- [19] L. Holleis, C. L. Patterson, Y. Zhang, Y. Vituri, H. M. Yoo, H. Zhou, T. Taniguchi, K. Watanabe, E. Berg, S. Nadj-Perge, and A. F. Young, *arXiv e-prints*, arXiv:2303.00742 (2023), arXiv:2303.00742 [cond-mat.supr-con].
- [20] C. Li, F. Xu, B. Li, J. Li, G. Li, K. Watanabe, T. Taniguchi, B. Tong, J. Shen, L. Lu, J. Jia, F. Wu, X. Liu, and T. Li, *Nature (London)* **631**, 300 (2024), arXiv:2405.04479 [cond-mat.supr-con].
- [21] P. A. Pantaleón, A. Jimeno-Pozo, H. Sainz-Cruz, V. T. Phong, T. Cea, and F. Guinea, *Nature Reviews Physics* **5**, 304 (2023), arXiv:2211.02880 [cond-mat.mes-hall].
- [22] A. M. Seiler, M. Statz, I. Weimer, N. Jacobsen, K. Watanabe, T. Taniguchi, Z. Dong, L. S. Levitov, and R. T. Weitz, *Phys. Rev. Lett.* **133**, 066301 (2024), arXiv:2308.00827 [cond-mat.str-el].
- [23] K. Huang, H. Fu, D. R. Hickey, N. Alem, X. Lin, K. Watanabe, T. Taniguchi, and J. Zhu, *Physical Review X* **12**, 031019 (2022), arXiv:2105.07058 [cond-mat.mes-hall].
- [24] L. Holleis, C. L. Patterson, Y. Zhang, Y. Vituri,

- H. M. Yoo, H. Zhou, T. Taniguchi, K. Watanabe, E. Berg, S. Nadj-Perge, and A. F. Young, *arXiv e-prints*, arXiv:2303.00742 (2023), arXiv:2303.00742 [cond-mat.supr-con].
- [25] H. Zhou, T. Xie, T. Taniguchi, K. Watanabe, and A. F. Young, *Nature (London)* **598**, 434 (2021), arXiv:2106.07640 [cond-mat.mes-hall].
- [26] S. Chatterjee, T. Wang, E. Berg, and M. P. Zaletel, *Nature Communications* **13**, 6013 (2022), arXiv:2109.00002 [cond-mat.supr-con].
- [27] T. Arp, O. Sheekey, H. Zhou, C. L. Tschirhart, C. L. Patterson, H. M. Yoo, L. Holleis, E. Redekop, G. Babikyan, T. Xie, J. Xiao, Y. Vituri, T. Holder, T. Taniguchi, K. Watanabe, M. E. Huber, E. Berg, and A. F. Young, *arXiv e-prints*, arXiv:2310.03781 (2023), arXiv:2310.03781 [cond-mat.mes-hall].
- [28] T. Han, Z. Lu, G. Scuri, J. Sung, J. Wang, T. Han, K. Watanabe, T. Taniguchi, L. Fu, H. Park, and L. Ju, *Nature (London)* **623**, 41 (2023), arXiv:2308.08837 [cond-mat.mes-hall].
- [29] C. L. Patterson, O. I. Sheekey, T. B. Arp, L. F. W. Holleis, J. M. Koh, Y. Choi, T. Xie, S. Xu, E. Redekop, G. Babikyan, H. Zhou, X. Cheng, T. Taniguchi, K. Watanabe, C. Jin, E. Lantagne-Hurtubise, J. Alicea, and A. F. Young, *arXiv e-prints*, arXiv:2408.10190 (2024), arXiv:2408.10190 [cond-mat.mes-hall].
- [30] W. Zhou, J. Ding, J. Hua, L. Zhang, K. Watanabe, T. Taniguchi, W. Zhu, and S. Xu, *Nature Communications* **15**, 2597 (2024), arXiv:2310.05319 [cond-mat.mes-hall].
- [31] J. M. Koh, A. Thomson, J. Alicea, and É. Lantagne-Hurtubise, *arXiv e-prints*, arXiv:2407.09612 (2024), arXiv:2407.09612 [cond-mat.mes-hall].
- [32] T. Wang, M. Vila, M. P. Zaletel, and S. Chatterjee, *Phys. Rev. Lett.* **132**, 116504 (2024), arXiv:2303.04855 [cond-mat.str-el].
- [33] Y. Zhumagulov, D. Kochan, and J. Fabian, *Phys. Rev. B* **110**, 045427 (2024), arXiv:2307.16025 [cond-mat.mtrl-sci].
- [34] Z. M. Raines, L. I. Glazman, and A. V. Chubukov, *arXiv e-prints*, arXiv:2406.04415 (2024), arXiv:2406.04415 [cond-mat.str-el].
- [35] Y.-C. Lee, D. V. Chichinadze, and A. V. Chubukov, *Phys. Rev. B* **109**, 155118 (2024), arXiv:2401.12384 [cond-mat.str-el].
- [36] Z. Dong, É. Lantagne-Hurtubise, and J. Alicea, *arXiv e-prints*, arXiv:2406.17036 (2024), arXiv:2406.17036 [cond-mat.supr-con].
- [37] J. H. Son, Y.-T. Hsu, and E.-A. Kim, *arXiv e-prints*, arXiv:2405.05442 (2024), arXiv:2405.05442 [cond-mat.str-el].
- [38] J. B. Curtis, N. R. Poniatowski, Y. Xie, A. Yacoby, E. Demler, and P. Narang, *Phys. Rev. Lett.* **130**, 196001 (2023), arXiv:2209.10560 [cond-mat.supr-con].
- [39] A. Jimeno-Pozo, H. Sainz-Cruz, T. Cea, P. A. Pantaleón, and F. Guinea, *Phys. Rev. B* **107**, L161106 (2023), arXiv:2210.02915 [cond-mat.mes-hall].
- [40] Y.-Z. Chou, F. Wu, J. D. Sau, and S. Das Sarma, *Phys. Rev. Lett.* **127**, 217001 (2021), arXiv:2105.00561 [cond-mat.supr-con].
- [41] Y.-Z. Chou, F. Wu, J. D. Sau, and S. Das Sarma, *arXiv e-prints*, arXiv:2204.09811 (2022), arXiv:2204.09811 [cond-mat.supr-con].
- [42] Z. Li, X. Kuang, A. Jimeno-Pozo, H. Sainz-Cruz, Z. Zhan, S. Yuan, and F. Guinea, *Phys. Rev. B* **108**, 045404 (2023), arXiv:2303.17286 [cond-mat.mes-hall].
- [43] G. Wagner, Y. H. Kwan, N. Bultinck, S. H. Simon, and S. A. Parameswaran, *arXiv e-prints*, arXiv:2302.00682 (2023), arXiv:2302.00682 [cond-mat.supr-con].
- [44] A. Ghazaryan, T. Holder, E. Berg, and M. Serbyn, *Phys. Rev. B* **107**, 104502 (2023), arXiv:2211.02492 [cond-mat.supr-con].
- [45] J. M. Koh, J. Alicea, and É. Lantagne-Hurtubise, *Phys. Rev. B* **109**, 035113 (2024), arXiv:2306.12486 [cond-mat.str-el].
- [46] D.-C. Lu, T. Wang, S. Chatterjee, and Y.-Z. You, *Phys. Rev. B* **106**, 155115 (2022), arXiv:2206.01213 [cond-mat.str-el].
- [47] V. Crépel and L. Fu, *Proceedings of the National Academy of Science* **119**, e2117735119 (2022), arXiv:2103.12060 [cond-mat.supr-con].
- [48] E. McCann and M. Koshino, *Reports on Progress in Physics* **76**, 056503 (2013), arXiv:1205.6953 [cond-mat.mes-hall].
- [49] E. McCann, Electronic properties of monolayer and bilayer graphene, in *Graphene Nanoelectronics: Metrology, Synthesis, Properties and Applications*, edited by H. Raza (Springer Berlin Heidelberg, Berlin, Heidelberg, 2012) pp. 237–275, arXiv:1205.4849 [cond-mat.mes-hall].
- [50] A. Friedlan and M. M. Dignam, *Phys. Rev. B* **103**, 075414 (2021).
- [51] F. Joucken, E. A. Quezada-López, J. Avila, C. Chen, J. L. Davenport, H. Chen, K. Watanabe, T. Taniguchi, M. C. Asensio, and J. Velasco, *Phys. Rev. B* **99**, 161406(R) (2019).
- [52] E. McCann, *Phys. Rev. B* **74**, 161403(R) (2006).
- [53] E. V. Castro, K. S. Novoselov, S. V. Morozov, N. M. R. Peres, J. M. B. Lopes dos Santos, J. Nilsson, F. Guinea, A. K. Geim, and A. H. Castro Neto, *Phys. Rev. Lett.* **99**, 216802 (2007).
- [54] Y. Zhang, T.-T. Tang, C. Girit, Z. Hao, M. C. Martin, A. Zettl, M. F. Crommie, Y. R. Shen, and F. Wang, *Nature* **459**, 820 (2009).
- [55] T. Ohta, A. Bostwick, T. Seyller, K. Horn, and E. Rotenberg, *Science* **313**, 951 (2006).
- [56] J. Y. Khoo, A. F. Morpurgo, and L. Levitov, *Nano Letters* **17**, 7003 (2017), arXiv:1711.04407 [cond-mat.mes-hall].
- [57] J. O. Island, X. Cui, C. Lewandowski, J. Y. Khoo, E. M. Spanton, H. Zhou, D. Rhodes, J. C. Hone, T. Taniguchi, K. Watanabe, L. S. Levitov, M. P. Zaletel, and A. F. Young, *Nature (London)* **571**, 85 (2019), arXiv:1901.01332 [cond-mat.mes-hall].
- [58] A. L. Szabó and B. Roy, *Phys. Rev. B* **105**, L201107 (2022).
- [59] Y.-Z. Chou, F. Wu, and S. Das Sarma, *Phys. Rev. B* **106**, L180502 (2022), arXiv:2206.09922 [cond-mat.supr-con].
- [60] S. Predin, P. Wenk, and J. Schliemann, *Phys. Rev. B* **93**, 115106 (2016), arXiv:1512.06556 [cond-mat.mes-hall].
- [61] G. W. Semenoff, *Phys. Rev. Lett.* **53**, 2449 (1984).
- [62] S. Y. Zhou, G. H. Gweon, A. V. Fedorov, P. N. First, W. A. de Heer, D. H. Lee, F. Guinea, A. H. Castro Neto, and A. Lanzara, *Nature Materials* **6**, 916 (2007), arXiv:0709.1706 [cond-mat.mtrl-sci].
- [63] D. Xiao, G.-B. Liu, W. Feng, X. Xu, and W. Yao, *Phys. Rev. Lett.* **108**, 196802 (2012), arXiv:1112.3144 [cond-

- [mat.mes-hall](#)].
- [64] C. Gong, H. Zhang, W. Wang, L. Colombo, R. M. Wallace, and K. Cho, *Applied Physics Letters* **103**, 053513 (2013), [arXiv:1308.0767 \[cond-mat.mtrl-sci\]](#).
- [65] H. Liu, P. Lazzaroni, and C. Di Valentin, *Nanomaterials* **8**, 481 (2018).
- [66] M. Gmitra and J. Fabian, *Phys. Rev. B* **92**, 155403 (2015).
- [67] Y. Li and M. Koshino, *Phys. Rev. B* **99**, 075438 (2019), [arXiv:1901.06769 \[cond-mat.mes-hall\]](#).
- [68] C. Puetter, H. Doh, and H.-Y. Kee, *Phys. Rev. B* **76**, 235112 (2007), [arXiv:0706.1069 \[cond-mat.str-el\]](#).
- [69] I. Khavkine, C.-H. Chung, V. Oganessian, and H.-Y. Kee, *Phys. Rev. B* **70**, 155110 (2004), [arXiv:cond-mat/0402565 \[cond-mat.str-el\]](#).